ARTICLES
https://doi.org/10.1038/s41558-022-01430-5

nature climate change

OPEN

Vertically migrating phytoplankton fuel high oceanic primary production

Kai Wirtz[1]✉, S. Lan Smith[2], Moritz Mathis[1] and Jan Taucher[3]

Marine net primary production (NPP) is remarkably high given the typical vertical separation of 50–150 m between the depth zones of light and nutrient sufficiency, respectively. Here we present evidence that many autotrophs bridge this gap through downward and upward migration, thereby facilitating biological nutrient pumping and high rates of oceanic NPP. Our model suggests that phytoplankton vertical migration (PVM) fuels up to 40% (>28 tg yr^{-1} N) of new production and directly contributes 25% of total oceanic NPP (herein estimated at 56 PgC yr^{-1}). Confidence in these estimates is supported by good reproduction of seasonal, vertical and geographic variations in NPP. In contrast to common predictions, a sensitivity study of the PVM model indicates higher NPP under global warming when enhanced stratification reduces physical nutrient transport into the surface ocean. Our findings suggest that PVM is a key mechanism driving marine biogeochemistry and therefore requires consideration in global carbon budgets.

Annual rates of net primary production (NPP) in the ocean typically exceed 50 gC m^{-2} yr^{-1} (refs. [1,2]). Prevalence of high NPP rates, however, disagrees with the widespread observation in low and middle latitudes of nutrient depletion in the upper water column where light intensity suffices for high photosynthesis rates. Saturating light conditions rarely extend deeper than 30–60 m, which in vast areas of the oligotrophic ocean is roughly 100 m above the nutrient-rich chemocline. This separation of the sunlit zone from the chemocline challenges unicellular autotrophs, which are believed to be short-lived and therefore to require light and nutrients simultaneously. Furthermore, high NPP rates near the surface sustain a continuous export flux out of the euphotic zone, which must be counterbalanced by nutrient inputs. However, diffusive fluxes from the nutrient-rich deep layers are often limited by a stratified pycnocline, which typically lies above the chemocline[3]. Lateral transport has been suggested by modelling studies as a nutrient source for the surface layer of oligotrophic gyres, but inorganic nutrients such as nitrate were simulated to enter only the margins of the gyres[4]. Finally, atmospheric nutrient deposition and N fixation by cyanobacteria provide roughly 10% to and maximum of 50% of the export flux and hence are insufficient to sustain productivity[5–8], especially since phosphorus deposition rates are negligibly low[9].

Therefore, conventional biogeochemical (BGC) models partially require weakly supported assumptions to reproduce high regional or global NPP rates (Supplementary Section 4), while detailed examinations of model results[10,11] and observations[5,9] suggest a substantial unknown source of nutrients to the surface layers.

One such alternative transport mechanism could be biological pumping by phytoplankton, carrying assimilated nutrients and migrating from the chemocline towards the surface. Vertical migration in the ocean has long been known for a few, fast-moving taxa such as mat-forming diatoms, dinoflagellates and the cyanobacterium *Trichodesmium*[12–15] but has so far not been included in global BGC modelling because of the limited abundance of those taxa. A much greater relevance of biological pumping has recently been proposed to follow from slow but long-term continuous migration over the scale of days and weeks by the large fraction of motile phytoplankton within the autotrophic community[16]. A Lagrangian model for phytoplankton vertical migration (PVM) applied at several marine stations indicated that substantial amounts of nutrients can be pumped up by migrating bulk phytoplankton.

In this Article, we test whether PVM can solve the enigma of high NPP rates in the nutrient-depleted surface ocean. We assess its relevance for global nutrient and carbon cycles and, more specifically, quantify the total amount of oceanic NPP facilitated by vertical migration and bio-pumping, both for present-day climatic conditions and in a warming future ocean.

Our model differentiates between two fractions of the phytoplankton community: vertical migrators (typically eukaryotes) and passive drifters (many prokaryotes)[16]. Immobile cells grow in the euphotic zone according to local light conditions while assuming moderate limitation by remineralized, deposited or fixed nitrogen and co-limitation by other nutrients as approximated by residual surface nitrate (Methods). Mobile cells are described as active Lagrangian particles, which are individual objects moving along a trajectory. In our model, cells commute between the chemocline, where they increase their nutrient/C ratios, and the upper sunlit layers, where photosynthetic carbon assimilation and utilization of stored nutrients reduce those ratios (Fig. 1). The biological upward N flux is quantified as the bulk concentration of intracellular nitrogen within mobile autotrophs above the chemocline times their mortality rate. The Lagrangian model is driven by time-dependent environmental conditions such as temperature and chemocline depth, as well as measured concentrations of chlorophyll (CHL) and nitrate at the surface (Methods, Supplementary Fig. 1 and ref. [16]). In the present study, these input data are processed in two different set-ups. First, applications to the monitoring stations Bermuda Atlantic Time Series (BATS), Hawaii Ocean Time Series (HOT), Northwest Pacific subarctic (K2) and Northwest Pacific subtropical (S1) test the validity of our approach with respect to NPP profiles under variable but directly monitored environmental conditions. Second, for a global application, we compiled the present-day climatological seasonality of environmental data at a spatial resolution of 0.5°. In this global set-up, the impact of vertical migration is also evaluated in a sensitivity study using changes in chemocline depth

[1]Helmholtz Zentrum Hereon, Geesthacht, Germany. [2]Earth SURFACE System Research Center, Research Institute for Global Change, JAMSTEC, Yokosuka, Japan. [3]GEOMAR Helmholtz Centre for Ocean Research Kiel, Kiel, Germany. ✉e-mail: kai.wirtz@hereon.de

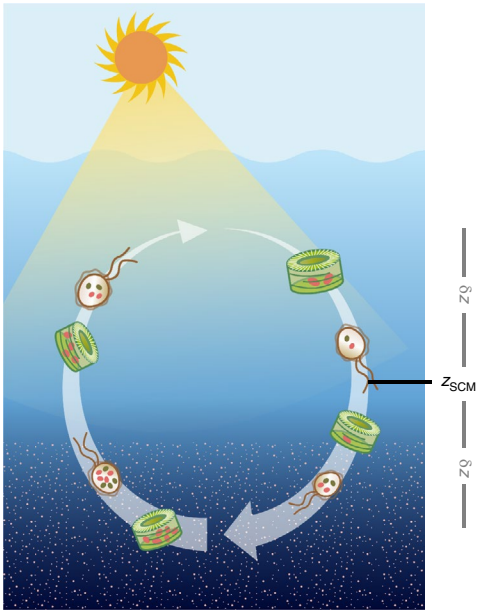

Fig. 1 | Biological nutrient pumping by vertically migrating phytoplankton cells. Cells with low intracellular nutrient content (indicated by small ellipses) settle or swim down to the chemocline while nutrient-rich cells ascend to the sunlit surface layers. Their vertical habitat spans from $z_{SCM} - \delta z$ to $z_{SCM} + \delta z$ with the average position z_{SCM} marking the depth of the subsurface chlorophyll maximum and vertical distance δz the migration amplitude. The up and down migration leads to a separation of cells having low versus high nutrient/C ratios at the same depth, depending only on their migration history. This separation is difficult to observe in situ and impossible to resolve in the Eulerian grid representation of conventional BGC models.

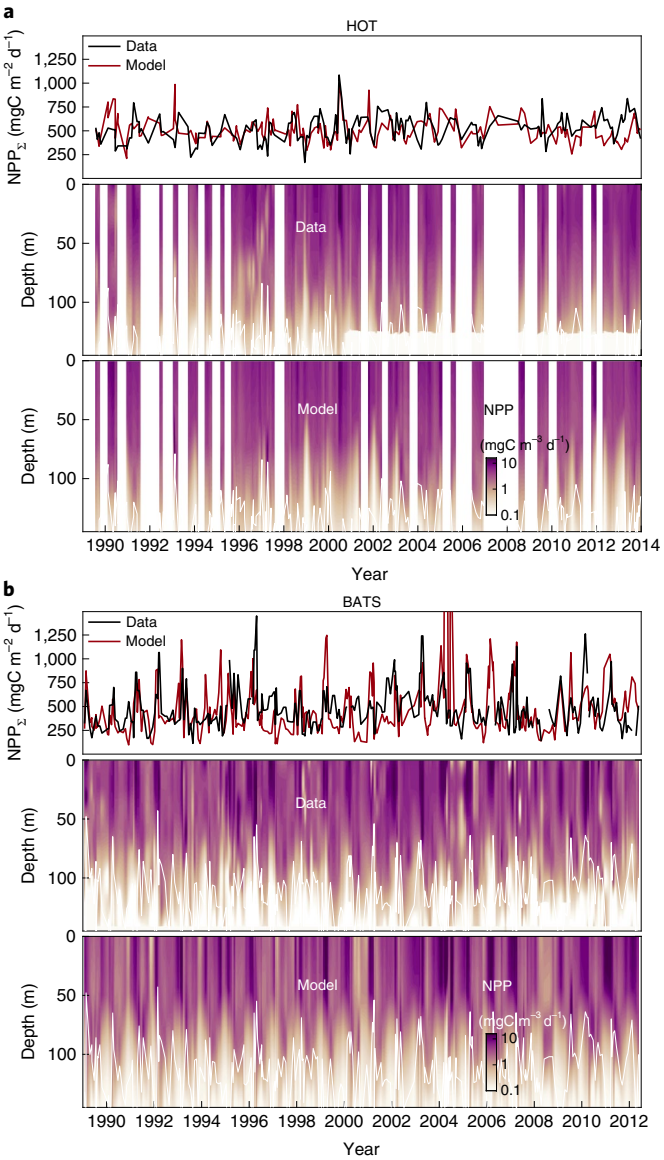

Fig. 2 | Comparison of simulated and observed variability in NPP. a,**b**, Contour plot of depth-resolved NPP from 1989 to 2014 observed at HOT (**a**) and from 1989 to 2012 observed at BATS (**b**), both compared with the model reconstruction. Measured and calculated NPP_Σ are displayed in the upper panels.

as projected by a global Earth system model under a global warming scenario (Supplementary Fig. 1).

Effect on global NPP and nutrient inputs

Our account of PVM reproduces well the observed NPP profiles at the four marine stations (agreement between climatological profiles of model results and observations in Extended Data Fig. 1), especially at HOT and BATS (Fig. 2), and also depth-integrated NPP (NPP_Σ) calculated in the global set-up (Extended Data Fig. 2), as described in Supplementary Section 1. The global simulation also generates reasonable seasonal variations in NPP_Σ in mid and high latitudes (Extended Data Fig. 3), with PVM contributing most to annual NPP at low latitudes (Fig. 3a). Despite a systematic underestimation in coastal seas and upwelling regions (Supplementary Section 1), the annual global rate of 56 PgC yr^{-1} calculated here exceeds current empirical estimates such as 49 PgC yr^{-1} by ref. [2] or 52 PgC yr^{-1} by ref. [17].

Simulated NPP decreases substantially in a control model variant neglecting PVM (Fig. 3b), especially in the tropical oceans, except for the Arabian Sea and western Central Atlantic. Without vertical migration, our model predicts a global oceanic NPP of 41 PgC yr^{-1}, 25% lower than the prediction with migration (Extended Data Fig. 4), which is in the upper range of the 7–28% contributions by migrating primary producers previously calculated for the reference stations[16].

However, for about one-third of the PVM areas, migration speeds below 0.7 m d^{-1} and migration distances below 12 m were obtained (Extended Data Figs. 5–7). At such low speeds and distances, active transport can hardly be distinguished from physical transport by diffusion. In these cases, the subsurface chlorophyll maximum (SCM) may indeed be dominated by non-migrating phytoplankton, especially when the CHL concentration at the SCM exceeds the one at the surface by a factor of only 1–3. This means that our estimated relative contributions by migrating primary producers should be taken as an upper threshold.

In addition to direct enhancements of NPP, substantial nutrient pumping by migrating phytoplankton fuels regenerated production by passively drifting phytoplankton. Biological pumping contributes an upward nutrient flux of about 5–10 mmol m^{-2} d^{-1} N in vast areas of the global ocean (Extended Data Fig. 8), which exceeds by more than an order of magnitude the estimates of combined atmospheric inputs (N deposition and N_2 fixation)[18] or of the particulate export flux[19]. Nevertheless, biological nutrient pumping generally extends tens of metres above the chemocline (see migration distance $2\delta z$ in Extended Data Fig. 5) and hence only partially reaches the surface zone where most NPP_Σ occurs. Therefore, we

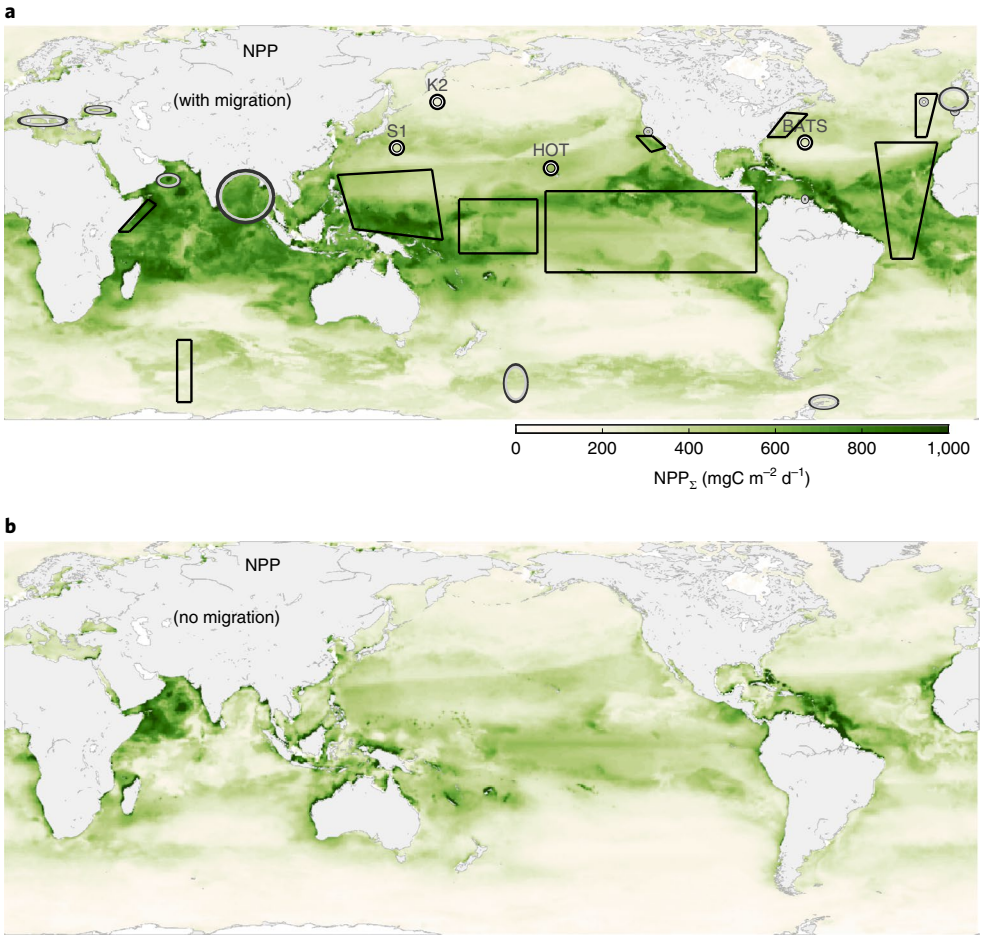

Fig. 3 | Simulated annual NPP$_\Sigma$. a, NPP$_\Sigma$ calculated with PVM switched on. **b**, NPP$_\Sigma$ with PVM switched off. These applications were fed by global fields of incident surface light, water temperature and chemocline depth (Methods). Circles, ellipses and polygons in **a** mark time-series stations and monitored areas referenced in the model–data comparison in Extended Data Fig. 2.

rescaled the pumping flux according to its vertical overlap with the productive zone: at each grid cell of the model, the flux is multiplied with the fraction of the total local NPP$_\Sigma$ realized within the vertical range of bio-pumping (the relative amount of NPP below $z_{SCM} - \delta z$). This rescaling yields an 'effective' global flux of 28 Tg yr^{-1} N. For comparison, 17 Tg yr^{-1} N is currently estimated for fluvial inflows, 39 Tg yr^{-1} N for net global deposition and 69 Tg yr^{-1} N for new production[18].

Uplifting the SCM

Indirect evidence for the existence of bulk PVM originates from the observed accumulation of CHL at depths substantially shallower than the nutrient-rich chemocline depth zN (Fig. 4). Although the photo-acclimative variation of CHL/C ratios, which our model includes, may determine SCM formation to a large extent[20], as also reproduced by photo-acclimation models[21,22], this systematic uplift of SCM depths above the chemocline is difficult to explain without migration. A version of our model neglecting migration predicts SCM near the chemocline, with $z_{SCM} \approx 0.9\ (z_N)$ (Supplementary Fig. 3). In the reference run of the model, migration confers greater advantage as the chemocline deepens, so that displacements strongly increase for $z_N > 100$ m. This pattern quantitatively agrees with data merged from the four open-ocean time-series stations (Fig. 4). SCM centre positions (z_{SCM}) 20–50 m above the chemocline are also frequently observed at other sites, such as in the Atlantic gyres[23], or are found to be representative for $z_{SCM} > 100$ m (ref. [24]).

Simulations including migration generate a nonlinear relation between z_{SCM} and z_N, which is identical to the observed pattern (statistically fitted relationships are not distinguishable, Fig. 4). A very similar relationship, including a threshold around $z_N = 100$ m, appears in an independent dataset covering the global ocean[2], supporting the generality of the SCM displacement. This uplifting extends the classical view of the SCM as located near the top of the chemocline, which was based mainly on data for $z_{SCM} < 100$ m (ref. [20]). SCM formation in situations with $z_N > 100$ m cannot be seamlessly reproduced by classical models using realistic parameterizations for light attenuation by water and particles and light affinity of autotrophs. Indeed, BGC models have not yet satisfactorily reproduced profiles at BATS and HOT despite the prominence of those extensive time-series observations. An exception was the early study of Doney et al.[10], who used a climatology of BATS data before 1993. In these years, chemocline was at times unusually shallow (Fig. 2), so that averaged z_N was around only 80–90 m. Similarly, station K2 in general has relatively low z_N, for which our model predicts a small contribution of active migration. The model study by Li et al.[25], which did not account for vertical migration, showed overall good skill in resolving subsurface CHL concentrations and SCM positioning at K2 (Supplementary Section 1). Like many models such as the one of Li et al.[25], our model resolves flexible CHL/C ratios (for example, with a typical increase by a factor 2.5 from the surface to 150 m depth; Supplementary Fig. 5[16]), which facilitate the development of an SCM and overall predict a decreasing biomass of non-migratory

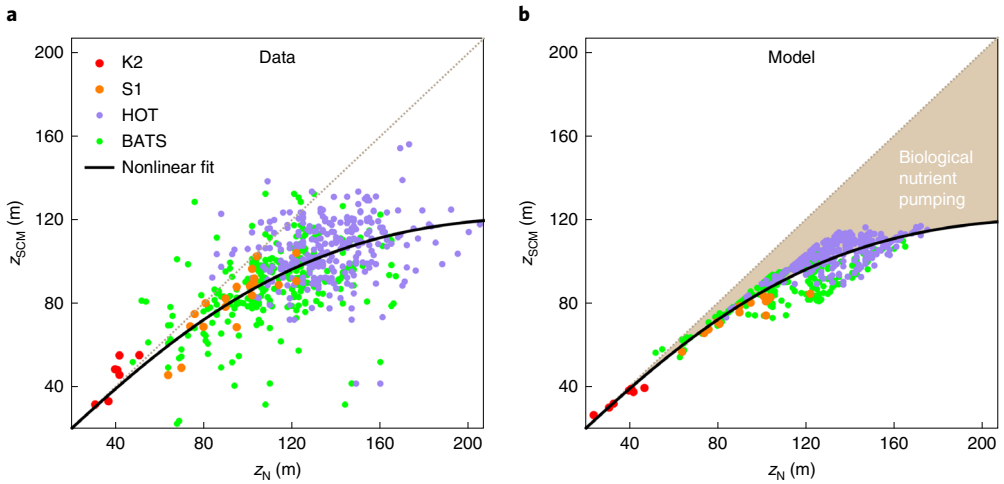

Fig. 4 | Relation between z_N and z_{SCM}. Empirically derived z_N and both simulated and observed z_{SCM} are shown for individual events at the marine time-series stations K2, S1, HOT and BATS. The relationship has been fitted using the function $y = x/(1 + (x/x^*)^2)$ (black line). **a**, z_{SCM} reconstructed from reported CHL profiles. Optimal fit parameter $x^* = 242$ m. **b**, z_{SCM} calculated by the model and fit function with $x^* = 240$ m.

Table 1 | Overview of phytoplankton mobility

Active locomotion	Buoyancy regulation
Of non-silicified species, 59% are flagellated[31] and thus capable of active locomotion. Even strains of aflagellated *Synechococcus* can actively swim[41,42]. Known responses to external cues comprise gravitaxis and phototaxis[43,44] and the capability to escape the control by turbulence[44].	Most diatoms and some cyanobacteria such as *Trichodesmium*[15] can regulate excess cell density. Buoyancy regulation using vacuoles within the protoplast and intracellular lipid storage is physiologically triggered by energetic status and nutrient content[45].
Dino-; crypto-; hapto-; raphido-; chloro-phyceae; dictyochales	Diatoms; cyanobacteria; haptophyceae
Some small species (<7 µm) with swimming speed >23 m d^{-1} (refs. [46–48]); effective migration speeds of small dinoflagellates (<17 µm) nearly equal swimming speeds[49]	Positive buoyancy unclear for sub-dominant group of small diatoms (<10 µm)
Prevalent migration speed of 0.4–4 m d^{-1} (refs. [45,50–52])	
Larger or colony-/chain-forming species with 50–100 m d^{-1} or more (refs. [13,14,46,49,52,53])	
Bulk vertical migration over distance of tens of metres (this study)	

Mobility traits and taxonomic relations are listed for active swimmers (left) and species using positive and negative buoyancy (right).

autotrophs with depth and a relatively small variation in the concentration of total phytoplankton C over depth down to the SCM, in agreement with a recent synthesis of particle backscatter data[24].

Fundamental traits shaping global biogeography and diversity

Active locomotion or buoyancy regulation is found in more than two-thirds of phytoplankton species (Table 1). Another ubiquitous trait is high plasticity in nutrient/carbon ratios. These and further evidences support the widespread existence and relevance of PVM (Supplementary Section 2). Our simulation suggests that most PVM is realized at migration speeds (v) below 1 m d^{-1}, thus well within the capability range of motile/buoyant species (Extended Data Fig. 6 and Table 1). Yet rapid migration at v above 10 m d^{-1} (Extended Data Fig. 7) is simulated in areas with low NPP_Σ (Fig. 3 and Extended Data Fig. 6), in proximity to the coast or with $z_{SCM} > 120$ m (Extended Data Fig. 9). In particular, the combination of high migration speed and deep SCM can lead to migration distances of up to 80–100 m (Extended Data Fig. 5). Diel, long-range migration of phytoplankton in coastal proximity, is in agreement with observed migration of dinoflagellates in Oslo fjord[13] and can be inferred from the dominance of huge diatoms and dinoflagellates in the North Arabian Sea[26], from high relative dinoflagellate abundance in the Yellow Sea[27] or the Timor Sea[28] or from recurrent cyanobacteria and dinoflagellate blooms in the Baltic Sea[29–31]. For offshore areas, moderately elevated average speeds in the subtropical Pacific (4–10 m d^{-1}) well correspond to the presence of buoyant diatom mats north of Hawaii[32].

However, the two traits z_{SCM} and v turn out to be rather independent at the global scale. Major subtropical bands with deep z_{SCM} (Extended Data Fig. 9) coincide very well with results of global compilations of SCM depths based on in situ data from ARGO floats[24,33], which document depths in the range 30–75 m for latitudes below 30° S, 75–145 m for 30–20° S, 50–75 m for 10° S–10° N, 50–120 m for 20–40° N and 20–40 m above 50° N. The subtropical bands in our simulation feature only a few patches where the phytoplankton community is dominated by fast-moving forms or where migration distances exceed 60–80 m. The independence of the behavioural traits determining different aspects of vertical migration strategy (centre, amplitude and speed) indicate the existence of many behavioural niches, which can be considered one component of the astounding diversity of phytoplankton[16].

Unexpected response to climate change

The distribution of functional traits well determines how the phytoplankton community reacts to environmental change[31,34]. The

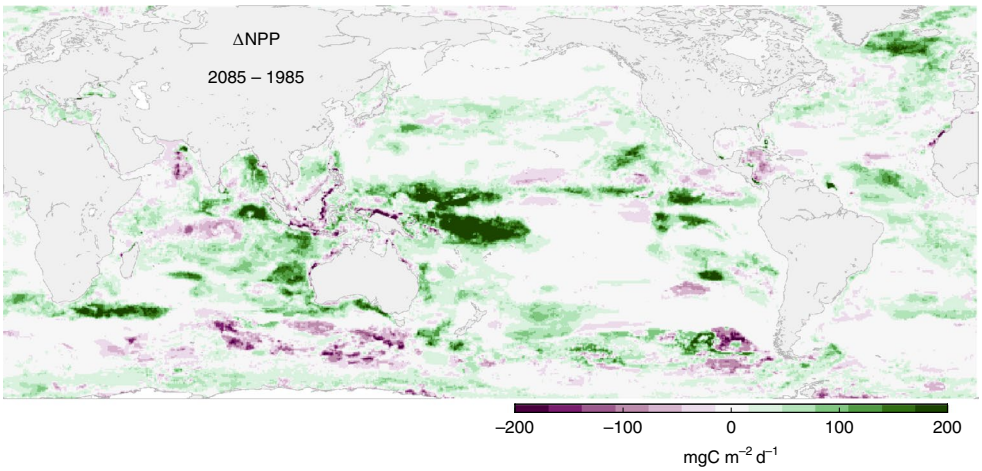

Fig. 5 | Change in NPP_Σ of the global ocean between time slices. NPP_Σ calculated by the model when the chemocline depths representing the recent past (1971–2000, '1985') are altered on the basis of a scenario simulation by the MPI-ESM for 2071–2100 ('2085').

biogeography of behavioural traits together with the relevance of phytoplankton behaviour compared with physical transport mechanisms may therefore be important for understanding the response of marine ecosystems to external drivers. This motivated us to conduct a sensitivity study of our global application related to a global change scenario.

Oceanic production has been suggested to decrease under anticipated climate change. Warming of surface waters, increasing stratification and, concomitantly, reduced nutrient supply from deeper layers may cause NPP to decrease[35]. In a projection by the Max-Planck-Institute (MPI) Earth system model (ESM; low-resolution (LR) Coupled Model Intercomparison Project 5 (CMIP5) version) within the emission scenario representative concentration pathway (RCP) 8.5[36], mixed-layer depth (MLD) overall decreases—with few exceptions (Supplementary Fig. 8), and within a century (from the time slice 1971–2000 to 2071–2100), the corresponding simulated oceanic production decreases by 8.5 PgC yr^{-1} (14%; Supplementary Fig. 5). This projection of enhanced stratification and reduced production lies well within the CMIP5 multimodel ensemble spread[35,37,38]. Accordingly, our model calculates lower NPP_Σ by non-migrating phytoplankton as a result of a lower thickness of the productive water layer, but also increased subsurface productivity due to uplifted SCM and migratory phytoplankton (Supplementary Figs. 1 and 3). This pattern is substantiated using a simple but also more mechanistic one-dimensional (1D) set-up where we iteratively run the Lagrangian PVM model with a Eulerian coupled physical–biological model, which resolves major nutrient sources and sinks such as uptake by all phytoplankton groups, N_2 fixation, regeneration and turbulent diffusive mixing (Supplementary Section 5). In this 1D set-up, altered temperature and wind forcing induces steeper vertical temperature gradient and a reduction of both biomass and productivity of non-mobile phytoplankton and of the chemocline depth due to decreased mixing; however, a reduced chemocline depth also leads to an increase in the concentration of mobile phytoplankton, especially at intermediate depths (Supplementary Fig. 6). In the global 3D application, substantial chemocline shallowing predicted for the Antarctic Circumpolar Current, North Pacific Current and North Atlantic areas south of the Greenland Current (Supplementary Figs. 7 and 8) induces only minor to moderate changes in NPP_Σ because relatively high CHL concentrations at the surface (Supplementary Fig. 9) disadvantage vertical migration as a viable strategy. By contrast, the changed distribution of chemocline depths translates to much enhanced growth of vertically migrating species in regions that combine low surface CHL (in our approach, equivalent to a small standing stock of drifters) with an intermediate SCM depth of 40–60 m. For example, in the North Equatorial Current, the western South Equatorial Current, the eastern Indian Ocean, the East Greenland Current and the region between the Agulhas and the Antarctic Circumpolar Current, even moderate decreases in chemocline depth (Supplementary Fig. 8) widen the habitat of vertically migrating species towards the sunlit surface layers (Extended Data Fig. 10) and, consequently, enhance their production rates. Overall, increased NPP_Σ by migrating phytoplankton more than compensates the decreased NPP_Σ by non-migrating phytoplankton (Fig. 5), leading to an increase in global oceanic NPP from 56.1 (in the reference run) to 58.4 PgC yr^{-1}. Some of the hotspots of NPP increase are proximate to regions where conventional models, including the MPI-ESM-LR, predict the greatest NPP decline[35], such as the Equatorial Countercurrent (Supplementary Fig. 5). The opposing responses of ESMs and our model to the same physical forcing challenges currently widespread approaches to predicting climate change effects.

A common strategy for sequential multi-resource acquisition

Phytoplankton is in most observational studies and in almost all coupled BGC models considered a passive tracer, lacking behavioural response. Consequences of neglecting phytoplankton migration in both satellite-based and mechanistic models are briefly discussed in Supplementary Section 4. In lakes, vertical migration by phytoplankton at high speed or over short distances was suggested earlier as an efficient strategy to enhance production, as summarized in Supplementary Section 3. Similarly, vertical migration observed for many crustaceans and other zooplankton taxa has been interpreted as an adaptive strategy in terms of both predator avoidance and resource exploitation[39]. A wide variety of organisms within the pelagic zone, such as cetaceans, employ migration to acquire multiple resources at distinct vertical positions. Even in ocean sediments, bacteria move up and down to obtain nitrate from above and sulfide from below[40]. Our study suggests that vertical migration by bulk marine phytoplankton is an equally widespread form of such migratory acquisition strategies that has not received sufficient attention so far, particularly considering its global-scale implications.

Conclusions

Our study shows that vertical migration of bulk phytoplankton can substantially fuel high NPP in the nutrient-depleted surface ocean. While it remains technically challenging to confirm this mechanism

and its implications in situ, our model results may stimulate the development of new observational approaches for directly testing the presence of PVM. The results also suggest that the picture of phytoplankton as continually active drifters can explain observed vertical profiles as well as depth-integrated rates of NPP over a wide range of ocean regions much better than conventional models that represent phytoplankton as passive drifters. The vertical structure and functioning of pelagic ecosystems may therefore be controlled by phytoplankton behaviour to a much greater degree than previously thought and not solely by physical mechanisms such as nutrient supply via turbulent mixing. The substantial impact of this strategy found in our global NPP calculations points to a systematic underestimation of oceanic production, which probably exceeds our conservative estimate of 56 PgC yr^{-1}. Notably, biological nutrient pumping implies a counteracting NPP response to reduced physical mixing, which is relevant for assessing the response of the global ocean ecosystem to a warming future climate. Our results hence emphasize the need to revise classical grid-based model approaches and observational techniques by changing the perception of phytoplankton from passive to active drifters.

Online content

Any methods, additional references, Nature Research reporting summaries, source data, extended data, supplementary information, acknowledgements, peer review information; details of author contributions and competing interests; and statements of data and code availability are available at https://doi.org/10.1038/s41558-022-01430-5.

Received: 1 May 2021; Accepted: 27 June 2022;
Published online: 2 August 2022

References

1. Westberry, T., Behrenfeld, M., Siegel, D. & Boss, E. Carbon-based primary productivity modeling with vertically resolved photoacclimation. *Glob. Biogeochem. Cycles* **22** (2008).
2. Richardson, K. & Bendtsen, J. Vertical distribution of phytoplankton and primary production in relation to nutricline depth in the open ocean. *Mar. Ecol. Prog. Ser.* **620**, 33–46 (2019).
3. Oschlies, A. in *Ocean Modeling in an Eddying Regime* (eds Hecht, M. W. & Hasumi, H.) 115–130 (AGU, 2008).
4. Letscher, R. T., Primeau, F. & Moore, J. K. Nutrient budgets in the subtropical ocean gyres dominated by lateral transport. *Nat. Geosci.* **9**, 815–819 (2016).
5. Johnson, K. S., Riser, S. C. & Karl, D. M. Nitrate supply from deep to near-surface waters of the North Pacific subtropical gyre. *Nature* **465**, 1062–1065 (2010).
6. Fawcett, S. E., Lomas, M. W., Casey, J. R., Ward, B. B. & Sigman, D. M. Assimilation of upwelled nitrate by small eukaryotes in the Sargasso Sea. *Nat. Geosci.* **4**, 717–722 (2011).
7. Knapp, A. N., Casciotti, K. L., Berelson, W. M., Prokopenko, M. G. & Capone, D. G. Low rates of nitrogen fixation in eastern tropical South Pacific surface waters. *Proc. Natl Acad. Sci. USA* **113**, 4398–4403 (2016).
8. Böttjer, D. et al. Temporal variability of nitrogen fixation and particulate nitrogen export at station ALOHA. *Limnol. Oceanogr.* **62**, 200–216 (2017).
9. Gruber, N., Keeling, C. D. & Stocker, T. F. Carbon-13 constraints on the seasonal inorganic carbon budget at the BATS site in the northwestern Sargasso Sea. *Deep Sea Res. 1* **45**, 673–717 (1998).
10. Doney, S. C., Glover, D. M. & Najjar, R. G. A new coupled, one-dimensional biological–physical model for the upper ocean: applications to the JGOFS Bermuda Atlantic Time-series Study (BATS) site. *Deep Sea Res. 2* **43**, 591–624 (1996).
11. Ascani, F. et al. Physical and biological controls of nitrate concentrations in the upper subtropical North Pacific Ocean. *Deep Sea Res 2* **93**, 119–134 (2013).
12. Gran, H. H. in *Rapport* Vol. 56, 1–112 (Bureau du Conseil permanent international pour l'exploration de la mer, 1929).
13. Hasle, G. R. Phototactic vertical migration in marine dinoflagellates. *Oikos* **2**, 162–175 (1950).
14. Villareal, T. A. et al. Upward transport of oceanic nitrate by migrating diatom mats. *Nature* **397**, 423–425 (1999).
15. Villareal, T. & Carpenter, E. Buoyancy regulation and the potential for vertical migration in the oceanic cyanobacterium *Trichodesmium*. *Microb. Ecol.* **45**, 1–10 (2003).
16. Wirtz, K. & Smith, S. L. Vertical migration by bulk phytoplankton sustains biodiversity and nutrient input to the surface ocean. *Sci. Rep.* **10**, 1142 (2020).
17. Silsbe, G. M., Behrenfeld, M. J., Halsey, K. H., Milligan, A. J. & Westberry, T. K. The CAFE model: a net production model for global ocean phytoplankton. *Glob. Biogeochem. Cycles* **30**, 1756–1777 (2016).
18. Wang, W.-L., Moore, J. K., Martiny, A. C. & Primeau, F. W. Convergent estimates of marine nitrogen fixation. *Nature* **566**, 205–211 (2019).
19. Karl, D. M., Letelier, R., Hebel, D. V., Bird, D. F. & Winn, C. D. in *Marine Pelagic Cyanobacteria: Trichodesmium and Other Diazotrophs* (eds Carpenter, E. J. et al.) 219–237 (Springer, 1992).
20. Cullen, J. J. Subsurface chlorophyll maximum layers: enduring enigma or mystery solved? *Ann. Rev. Mar. Sci.* **7**, 207–239 (2015).
21. Masuda, Y. et al. Photoacclimation by phytoplankton determines the distribution of global subsurface chlorophyll maxima in the ocean. *Commun. Earth Environ.* **2**, 1–8 (2021).
22. Anugerahanti, P., Kerimoglu, O. & Smith, S. L. Enhancing ocean biogeochemical models with phytoplankton variable composition. *Front. Mar. Sci.* **8**, 675428 (2021).
23. Pérez, V., Fernández, E., Marañón, E., Morán, X. A. G. & Zubkov, M. V. Vertical distribution of phytoplankton biomass, production and growth in the Atlantic subtropical gyres. *Deep Sea Res. 1* **53**, 1616–1634 (2006).
24. Cornec, M. et al. Deep chlorophyll maxima in the global ocean: occurrences, drivers and characteristics. *Glob. Biogeochem. Cycles* **35**, e2020GB006759 (2021).
25. Li, Q. P., Wang, Y., Dong, Y. & Gan, J. Modeling long-term change of planktonic ecosystems in the northern South China Sea and the upstream Kuroshio Current. *J. Geophys. Res.* **120**, 3913–3936 (2015).
26. Latif, S., Ayub, Z. & Siddiqui, G. Seasonal variability of phytoplankton in a coastal lagoon and adjacent open sea in Pakistan. *Turk. J. Botany* **37**, 398–410 (2013).
27. Liang, Y. et al. Nutrient-limitation induced diatom–dinoflagellate shift of spring phytoplankton community in an offshore shellfish farming area. *Mar. Pollut. Bull.* **141**, 1–8 (2019).
28. Rahlff, J. et al. Short-term responses to ocean acidification: effects on relative abundance of eukaryotic plankton from the tropical Timor Sea. *Mar. Ecol. Prog. Ser.* **658**, 59–74 (2021).
29. Kahru, M., Savchuk, O. & Elmgren, R. Satellite measurements of cyanobacterial bloom frequency in the Baltic Sea: interannual and spatial variability. *Mar. Ecol. Prog. Ser.* **343**, 15–23 (2007).
30. Klais, R., Tamminen, T., Kremp, A., Spilling, K. & Olli, K. Decadal-scale changes of dinoflagellates and diatoms in the anomalous Baltic Sea spring bloom. *PLoS ONE* **6**, e21567 (2011).
31. Klais, R., Norros, V., Lehtinen, S., Tamminen, T. & Olli, K. Community assembly and drivers of phytoplankton functional structure. *Funct. Ecol.* **31**, 760–767 (2017).
32. Villareal, T. A., Pilskaln, C. H., Montoya, J. P. & Dennett, M. Upward nitrate transport by phytoplankton in oceanic waters: balancing nutrient budgets in oligotrophic seas. *PeerJ* **2**, e302 (2014).
33. Mignot, A. et al. Understanding the seasonal dynamics of phytoplankton biomass and the deep chlorophyll maximum in oligotrophic environments: a bio-argo float investigation. *Glob. Biogeochem. Cycles* **28**, 856–876 (2014).
34. Chen, B., Smith, S. L. & Wirtz, K. W. Effect of phytoplankton size diversity on primary productivity in the North Pacific: trait distributions under environmental variability. *Ecol. Lett.* **22**, 56–66 (2019).
35. Cabré, A., Marinov, I. & Leung, S. Consistent global responses of marine ecosystems to future climate change across the IPCC AR5 Earth system models. *Clim. Dyn.* **45**, 1253–1280 (2015).
36. Giorgetta, M. A. et al. Climate and carbon cycle changes from 1850 to 2100 in MPI-ESM simulations for the Coupled Model Intercomparison Project phase 5. *J. Adv. Mod. Earth Sys.* **5**, 572–597 (2013).
37. Bopp, L. et al. Multiple stressors of ocean ecosystems in the 21st century: projections with CMIP5 models. *Biogeosciences* **10**, 6225–6245 (2013).
38. Fu, W., Randerson, J. T. & Moore, J. K. Climate change impacts on net primary production (NPP) and export production (EP) regulated by increasing stratification and phytoplankton community structure in the CMIP5 models. *Biogeosciences* **13**, 5151–5170 (2016).
39. Gliwicz, M. Z. Predation and the evolution of vertical migration in zooplankton. *Nature* **320**, 746–748 (1986).
40. Huettel, M., Forster, S., Kloser, S. & Fossing, H. Vertical migration in the sediment-dwelling sulfur bacteria *Thioploca* spp. in overcoming diffusion limitations. *Appl. Environ. Microbiol.* **62**, 1863–1872 (1996).
41. Waterbury, J. B., Willey, J. M., Franks, D. G., Valois, F. W. & Watson, S. W. A cyanobacterium capable of swimming motility. *Science* **230**, 74–76 (1985).
42. McCarren, J. et al. Inactivation of *swmA* results in the loss of an outer cell layer in a swimming *Synechococcus* strain. *J. Bacteriol.* **187**, 224–230 (2005).
43. Eppley, R. W., Holm-Hansen, O. & Strickland, J. D. Some observations on the vertical migration of dinoflagellates. *J. Phycol.* **4**, 333–340 (1968).
44. Sengupta, A., Carrara, F. & Stocker, R. Phytoplankton can actively diversify their migration strategy in response to turbulent cues. *Nature* **543**, 555–558 (2017).

45. Waite, A., Fisher, A., Thompson, P. & Harrison, P. Sinking rate verses cell volume relationships illuminate sinking rate control mechanisms in marine diatoms. *Mar. Ecol. Prog. Ser.* **157**, 97–108 (1997).
46. Throndsen, J. Motility in some marine nanoplankton flagellates. *Nor. J. Zool.* **21**, 193–200 (1973).
47. Gittleson, S. M., Hotchkiss, S. K. & Valencia, F. G. Locomotion in the marine dinoflagellate *Amphidinium carterae* (Hulburt). *Trans. Am. Microsc. Soc.* **93**, 101–105 (1974).
48. Barsanti, L. et al. Swimming patterns of the quadriflagellate *Tetraflagellochloris mauritanica* (Chlamydomonadales, Chlorophyceae). *J. Phycol.* **52**, 209–218 (2016).
49. Schuech, R. & Menden-Deuer, S. Going ballistic in the plankton: anisotropic swimming behavior of marine protists. *Limnol. Oceanogr. Fluids Environ.* **4**, 1–16 (2014).
50. Eppley, R. W., Holmes, R. W. & Strickland, J. D. Sinking rates of marine phytoplankton measured with a fluorometer. *J. Exp. Mar. Biol. Ecol.* **1**, 191–208 (1967).
51. Bienfang, P. Phytoplankton sinking rates in oligotrophic waters off Hawaii, USA. *Mar. Biol.* **61**, 69–77 (1980).
52. Lisicki, M., Rodrigues, M. F. V., Goldstein, R. E. & Lauga, E. Swimming eukaryotic microorganisms exhibit a universal speed distribution. *Elife* **8**, e44907 (2019).
53. Moore, J. & Villareal, T. Buoyancy and growth characteristics of three positively buoyant marine diatoms. *Mar. Ecol. Prog. Ser.* **132** (1996).

Methods

Local and global model set-ups. We applied the Lagrangian model for PVM in two settings: a 1D set-up for each of the four time-series observation sites (BATS, HOT, K2 and S1) and a 3D set-up covering the global ocean. In both set-ups, the previously described PVM model[16] used the documented parameterization, except for an additional co-limitation term (see the following). Their major dependencies on boundary forcing, especially the response of PVM to variations in chemocline depth, are illustrated in Supplementary Figs. 1 and Fig. 3.

Forcing and validation of the model in the 1D set-up relied on publicly available data for vertical profiles of chlorophyll, nutrients and NPP as described in the predecessor study[16], which especially includes the NPP data from HOT[54] and BATS[55]. We also integrated downward short-wave radiation fluxes from the JRA55 re-analysis[56], aggregated to daily (24 h) values from the originally provided 3-hourly data. In addition, estimates for MLD available for HOT were used to better reconstruct seasonal variations in mixing lengths, which otherwise were calculated using sea surface temperature data (Supplementary Section 5[16]).

Forcing data for the 3D set-up originated from global datasets on a 0.5° grid. Nitrate profiles, covering the global ocean based on World Ocean Circulation Experiment and World Ocean Database 2009[57], were available through the CSIRO Atlas of Regional Seas (CARS2009) database[58]. Surface values $NO_{3,0}$ were directly extracted (Supplementary Fig. 4), whereas the profiles were further processed to z_N using the algorithm documented before[16] (see annual average in Supplementary Fig. 7). Surface chlorophyll (Supplementary Fig. 9), sea surface temperature and cloud cover were obtained from the European Space Agency Climate Change Initiative[59–61]. The datasets for the period 1999–2010 integrate observations from three satellites. All global boundary data were pooled into four seasonal time slices: December–February (DJF), March–May (MAM), June–August (JJA) and September–November (SON). Net short-wave radiation was calculated using an astronomical formula based on date, geographic position and cloud cover[62].

The global set-up was run for the four seasonal climatologies in three simulation experiments: (1) a reference run, (2) with PVM switched off and (3) with an altered chemocline field emulating a projected reduction in MLD in a future climate. These future changes in z_N were estimated using an RCP 8.5 climate change scenario run of the MPI-ESM-LR[36]. After re-gridding, absolute changes in MLD between the recent-past (1971–2000) and future (2071–2100) distributions were added to the existing distribution of chemocline depth. We chose MLD instead of z_N, which were both calculated by the MPI-ESM, because changes in MLD were responsible for changes in z_N, regardless of which specific BGC processes mediated those changes in the MPI-ESM. To avoid unrealistic adjustment, these differences in MLD were cut so that chemocline depths were altered by at most 50% (Supplementary Fig. 8). The consistency of this treatment was qualitatively confirmed by the alternative 1D set-up, which explicitly accounts for most processes shaping the nutrient profile, hence z_N, and for feedbacks between changed z_N, migration behaviour and ecosystem dynamics (Supplementary Fig. 6).

Optimization of migration traits. Active migration of unicellular autotrophs reflects tactic responses to external cues such as light as well as intracellular biochemical status[50,51,63], which some 1D rule-based models already include for fast-moving phytoplankton[63–66]. Our model assumes near optimality of the migration pathway or strategy, respectively[16]. A variable migration strategy is defined by average positioning (z_{SCM}), migration amplitude (vertical distance $2\delta z$, Fig. 1) and migration speed (v). A search algorithm identifies the optimal and near-optimal strategies in terms of net growth rate realized at a given environment (incident surface light, water temperature, surface CHL concentration, chemocline depth, surface nitrate concentration). The local optimization implies that the 3D global application neglects any lateral exchange. Local, close near-optimal strategies may follow from different migration pathways so that the averaged migration traits can already reflect an aggregation over diverse speeds or central positions.

Parameterization of co-limitation. The model has been modified from the original version[16] by adding a co-limitation factor f_{colim} for immobile producers depending on surface nitrate values $NO_{3,0}$ (=$NO_3(z=0)$, as part of the CARS2009 data[58]) (see the preceding; Supplementary Fig. 4). High $NO_{3,0}$ can indicate limitation by iron or other nutrients, which will lower phytoplankton growth and production rates proportional to f_{colim}. The factor is parameterized using the specific co-limitation variation f^0_{colim}: $f_{colim} = 1 - f^0_{colim} + f^0_{colim} \exp(-NO^2_{3,0})$.

Substantial residual surface nitrate has been observed at K2, where recurrent iron limitation has been reported. While the original model ($f^0_{colim}=0$) overestimates NPP_Σ at K2 (not shown), with our setting $f^0_{colim}=0.5$ it underestimates the observations. We decided to keep this parameterization because we aim at a conservative lower estimate of global NPP.

Data availability

All datasets used as model forcing are publicly available (see Methods).

Code availability

The MATLAB code required to produce all model results is available at https://doi.org/10.5281/zenodo.6608970.

References

54. *Hawaii Ocean Time-series (HOT)* (School of Ocean and Earth Science and Technology at the University of Hawai'i, 2020); http://hahana.soest.hawaii.edu/hot/hot-dogs
55. *Bermuda Atlantic Time-Series (BATS)* (Bermuda Institute of Ocean Sciences, 2020); http://bats.bios.edu
56. *The Japanese 55-Year Reanalysis (JRA-55)* (Japan Meteorological Agency, 2020); http://jra.kishou.go.jp/JRA-55
57. Ridgway, K., Dunn, J. & Wilkin, J. Ocean interpolation by four-dimensional weighted least squares—application to the waters around Australasia. *J. Atmos. Ocean. Technol.* **19**, 1357–1375 (2002).
58. *CSIRO Atlas of Regional Seas (CARS)* (CSIRO, 2009); http://www.marine.csiro.au/~dunn/cars2009
59. *Ocean Colour* (ESA-CCI, 2020); http://www.esa-oceancolour-cci.org
60. *Cloud* (ESA-CCI, 2020); http://www.esa-cloud-cci.org
61. *Sea Surface Temperature* (ESA-CCI, 2020); http://www.esa-sst-cci.org
62. Rosati, A. & Miyakoda, K. A general circulation model for upper ocean simulation. *J. Phys. Oceanogr.* **18**, 1601–1626 (1988).
63. Ralston, D. K., McGillicuddy, D. J. & Townsend, D. W. Asynchronous vertical migration and bimodal distribution of motile phytoplankton. *J. Plankton Res.* **29**, 803–821 (2007).
64. Kamykowski, D. & Yamazaki, H. A study of metabolism-influenced orientation in the diel vertical migration of marine dinoflagellates. *Limnol. Oceanogr.* **42**, 1189–1202 (1997).
65. Richardson, T. L., Cullen, J. J., Kelley, D. E. & Lewis, M. R. Potential contributions of vertically migrating *Rhizosolenia* to nutrient cycling and new production in the open ocean. *J. Plankton Res.* **20**, 219–241 (1998).
66. Ross, O. N. & Sharples, J. Phytoplankton motility and the competition for nutrients in the thermocline. *Mar. Ecol. Prog. Ser.* **347**, 21–38 (2007).
67. Chavez, F. P., Messié, M. & Pennington, J. T. Marine primary production in relation to climate variability and change. *Ann. Rev. Mar. Sci.* **3**, 227–260 (2011).
68. Saba, V. et al. An evaluation of ocean color model estimates of marine primary productivity in coastal and pelagic regions across the globe. *Biogeosciences* **8**, 489–503 (2011).
69. Bhattathiri, P., Devassy, V. & Radhakrishna, K. Primary production in the Bay of Bengal during southwest monsoon of 1978. *Mahasagar Bull. Natl Inst. Oceanogr.* **13**, 315–323 (1980).
70. Sarupria, J. & Bhargava, R. Seasonal primary production in different sectors of the EEZ of India. *Mahasagar Bull. Natl Inst. Oceanogr.* **26**, 139–147 (1993).
71. Jyothibabu, R. et al. Differential response of winter cooling on biological production in the northeastern Arabian Sea and northwestern Bay of Bengal. *Curr. Sci.* **87**, 783–791 (2004).
72. Kumar, S. P. et al. Is the biological productivity in the Bay of Bengal light limited? *Curr. Sci.* **98**, 1331–1339 (2010).
73. Kumar, S. P. et al. Seasonal cycle of physical forcing and biological response in the Bay of Bengal. *Ind. J. Mar. Sci.* **39**, 388–405 (2010).
74. Buitenhuis, E. T., Hashioka, T. & Quéré, C. L. Combined constraints on global ocean primary production using observations and models. *Glob. Biogeochem. Cycles* **27**, 847–858 (2013).

Acknowledgements

ESA, CSIRO and JMA are acknowledged for making their data available. The work was supported by the Helmholtz society via the programme 'Changing Earth'. K.W. was supported by the BMBF project Multiple Stressors on North Sea Life—MuSSeL with project no. 03F0862A; M.M. was supported by Germany's Excellence Strategy EXC2037 (CLICCS—Climate, Climatic Change and Society) with project no 390683824. We thank P. Anugerahanti and C. Völcker for sharing their model set-ups for the HOT station. We also acknowledge the contributions of the many scientists and technicians who produced and made available the data from the time-series observations at stations BATS, HOT, K2 and S1.

Author contributions

K.W. conceived and conducted the model experiments. S.L.S. and M.M. provided part of the validation and forcing data. K.W., S.L.S., J.T. and M.M. analysed the results and wrote the manuscript.

Funding

Open access funding provided by Helmholtz-Zentrum hereon GmbH (4216).

Competing interests

The authors declare no competing interests.

Additional information

Extended data is available for this paper at https://doi.org/10.1038/s41558-022-01430-5.

Supplementary information The online version contains supplementary material available at https://doi.org/10.1038/s41558-022-01430-5.

Correspondence and requests for materials should be addressed to Kai Wirtz.

Peer review information *Nature Climate Change* thanks Qian Li, Tracy Villareal and the other, anonymous, reviewer(s) for their contribution to the peer review of this work.

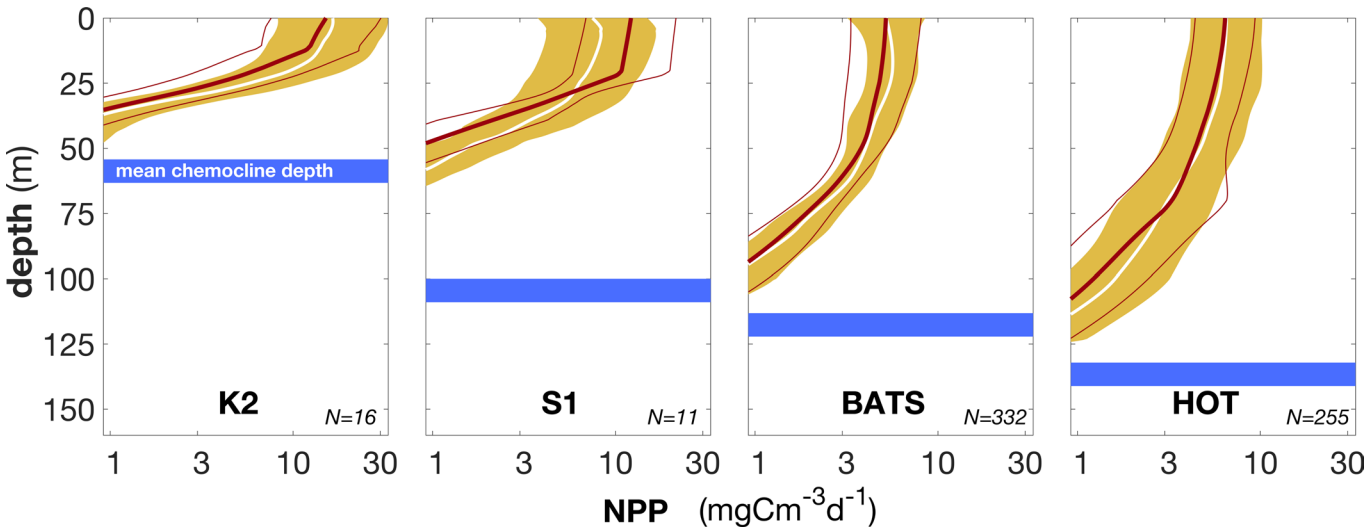

Extended Data Fig. 1 | Pooled profiles of NPP at four marine time-series stations. Pooled profiles of NPP at four marine time-series stations. Mean (white line) and standard deviation (colored area) of observations are plotted together with mean (thick color line) and standard deviation (thin color line) of simulated profiles for the stations subarctic West Pacific (K2), subtropic West Pacific (S1), Bermuda Atlantic Time-Series (BATS) and Hawaii Ocean Time-series (HOT). Mean chemocline depths are indicated by blue bars.

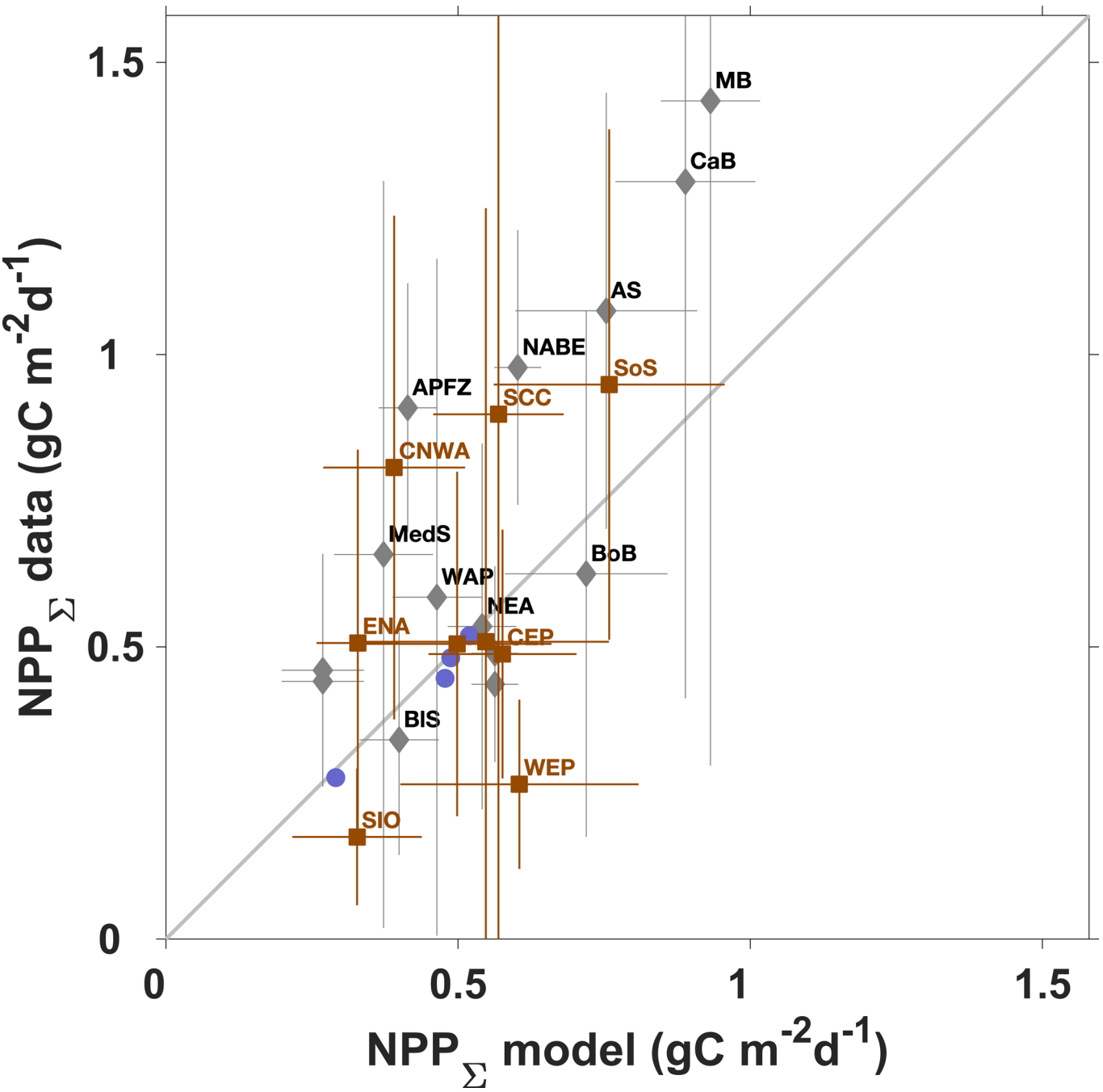

Extended Data Fig. 2 | Comparison of calculated and observed NPP$_\Sigma$. Comparison of calculated and observed NPP$_\Sigma$. Standard deviations represent temporal variability at the reference stations (S1, K2, HOT, and BATS, blue circles) or lateral variability for campaign data. Aggregated observational data (grey diamonds) derive from the compilations of (a) Chavez et al[67], (b) Saba et al[68], which also include values for HOT and BATS, and (c) our integration of cruise data for the Bay of Bengal[69–73]. Two extremely high values for coastal stations reported by Chavez et al were not plotted: La Coruna (LC, 1713 mg-Cm^{-2}d^{-1}), because the standard deviation exceeded the mean value, and Peru (3580 mg-Cm^{-2}d^{-1}) because of lacking error statistics. Very high values (>1150 mg-Cm^{-2}d^{-1}) reported for the BoB[73] were omitted as well. (d) Individual NPP profile data collected by Buitenhuis et al[74] were interpolated, summed to NPP$_\Sigma$, averaged for each season (depending on temporal coverage) and then compared to the polygon-averaged model data. Brown squares represent the mean of both seasonal series. Surrounding shapes for all campaign data are given as ellipses (a-c) or polygons (d) in Fig. 3a and Extended Data Fig. 3. Abbreviations: APFZ: Antarctic Polar Frontal Zone; AS: Arabian Sea; BlS: Black Sea; BoB: Bay of Bengal; CaB: Cariaco Basin; CEP: Central Equatorial Pacific; CNWA: Coastal Northwest Atlantic; EA: Eastern Central Atlantic; EEP: East Equatorial Pacific; ENA: Eastern North Atlantic; MB: Monterey Bay; Med: Mediterranean Sea; NABE: Northeast Atlantic Bloom Experiment; NEA: Northeast Atlantic; RS: Ross Sea; SCC: Southern California Current; SIO: Southern Indean Ocean; SoS: Somali Sea; WAP: West Antarctic Peninsula; WEP: Western Equatorial Pacific.

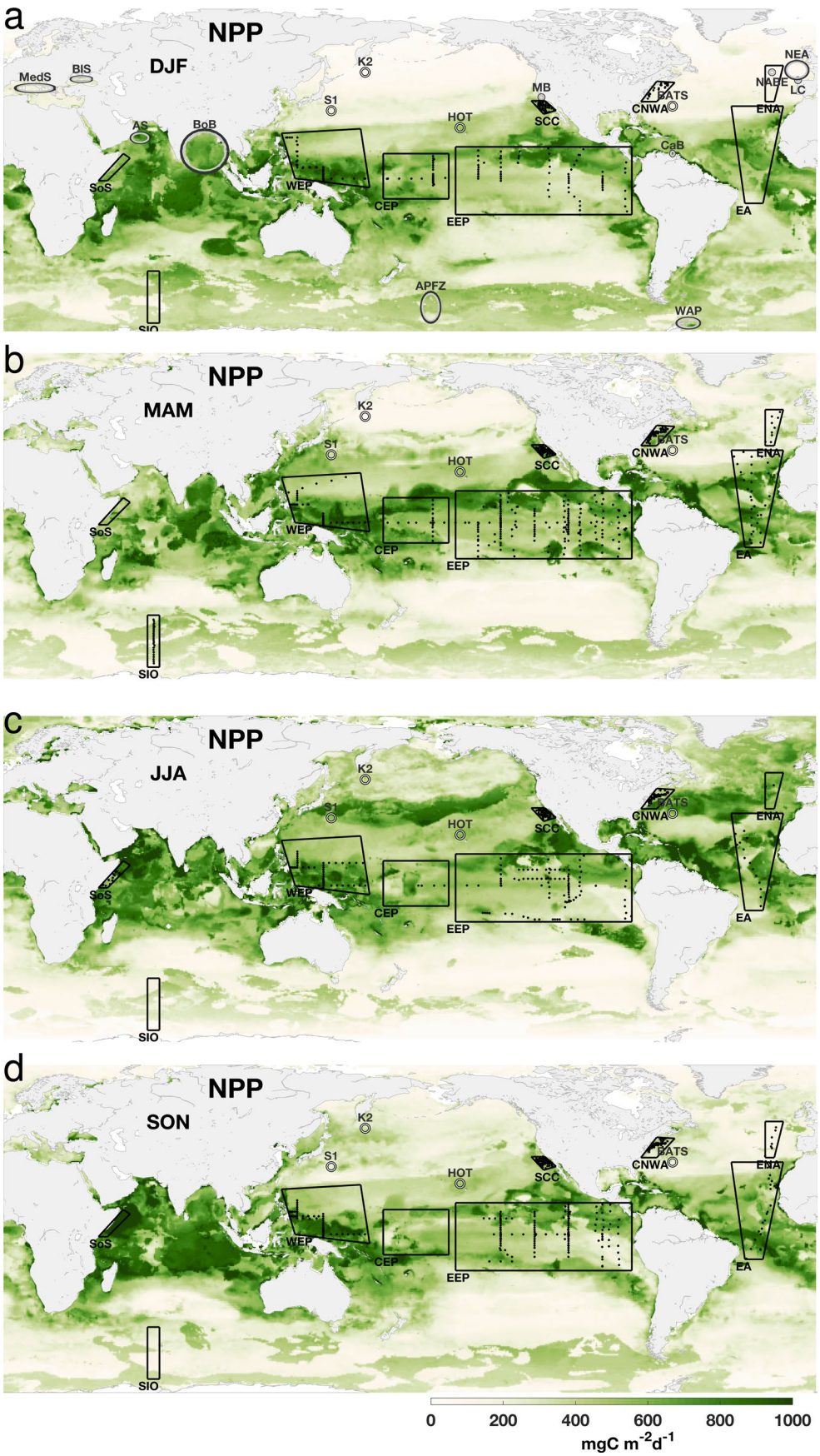

Extended Data Fig. 3 | Seasonal distribution of simulated NPP_{Σ}. Seasonal distribution of simulated NPP_{Σ}. a, for Dec-Feb. b, Mar-May. c, Jun-Aug. d, Sep-Nov. Dots within polygons represent individual profile data collected by Buitenhuis et al[74] (for abbreviations of site names see Extended Data Fig. 2).

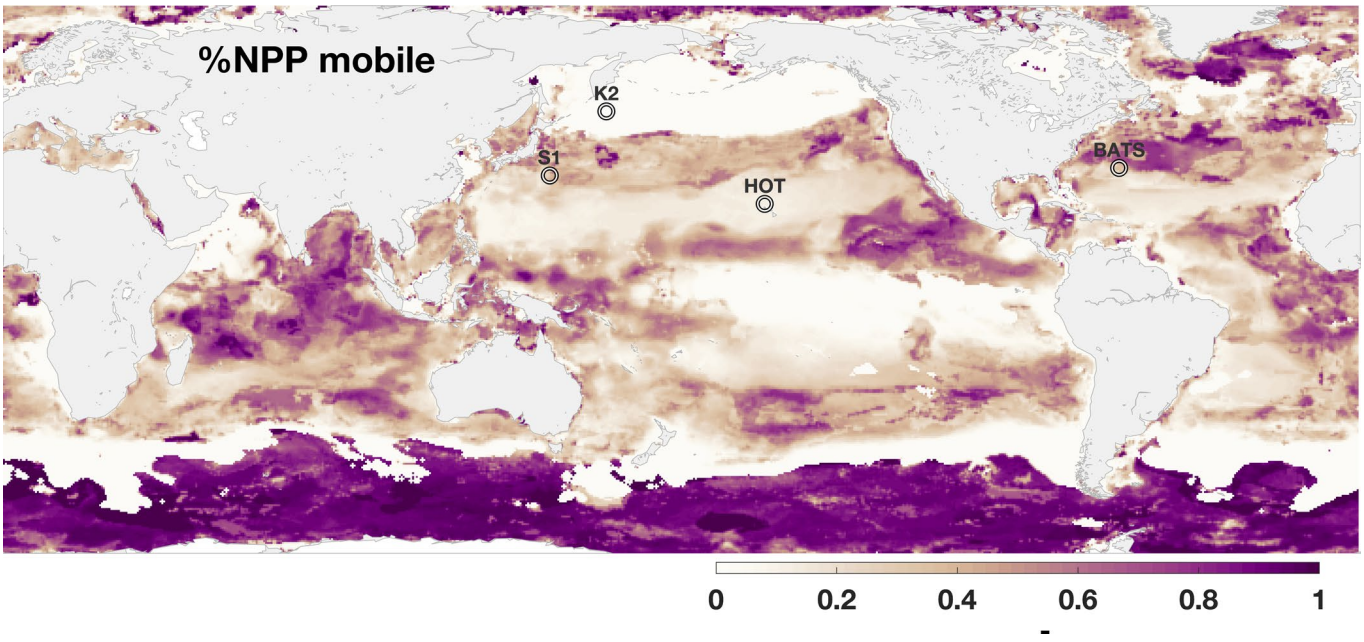

Extended Data Fig. 4 | Fraction of NPP_{Σ} mediated by migrating phytoplankton. Fraction of NPP_{Σ} mediated by migrating phytoplankton (annual mean).

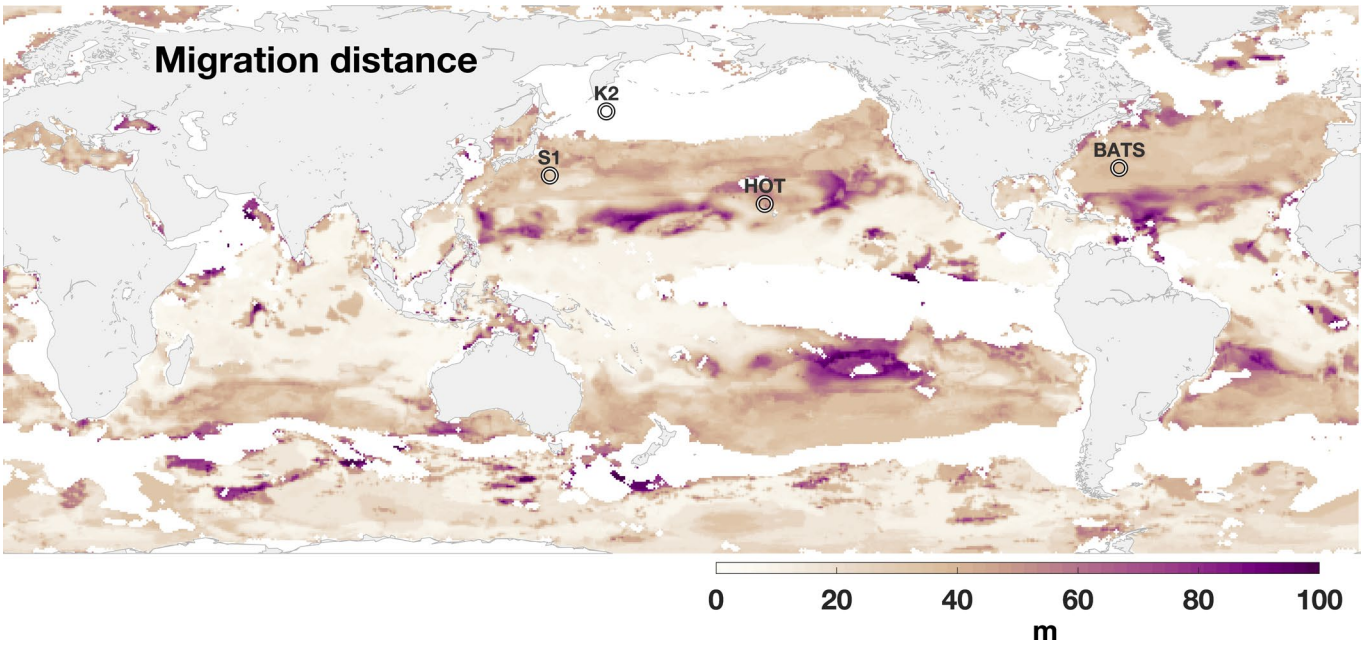

Extended Data Fig. 5 | Reconstructed migration distance $2\delta z$. Reconstructed migration distance $2\delta z$ (annual mean). White areas indicate absence of vertical migration.

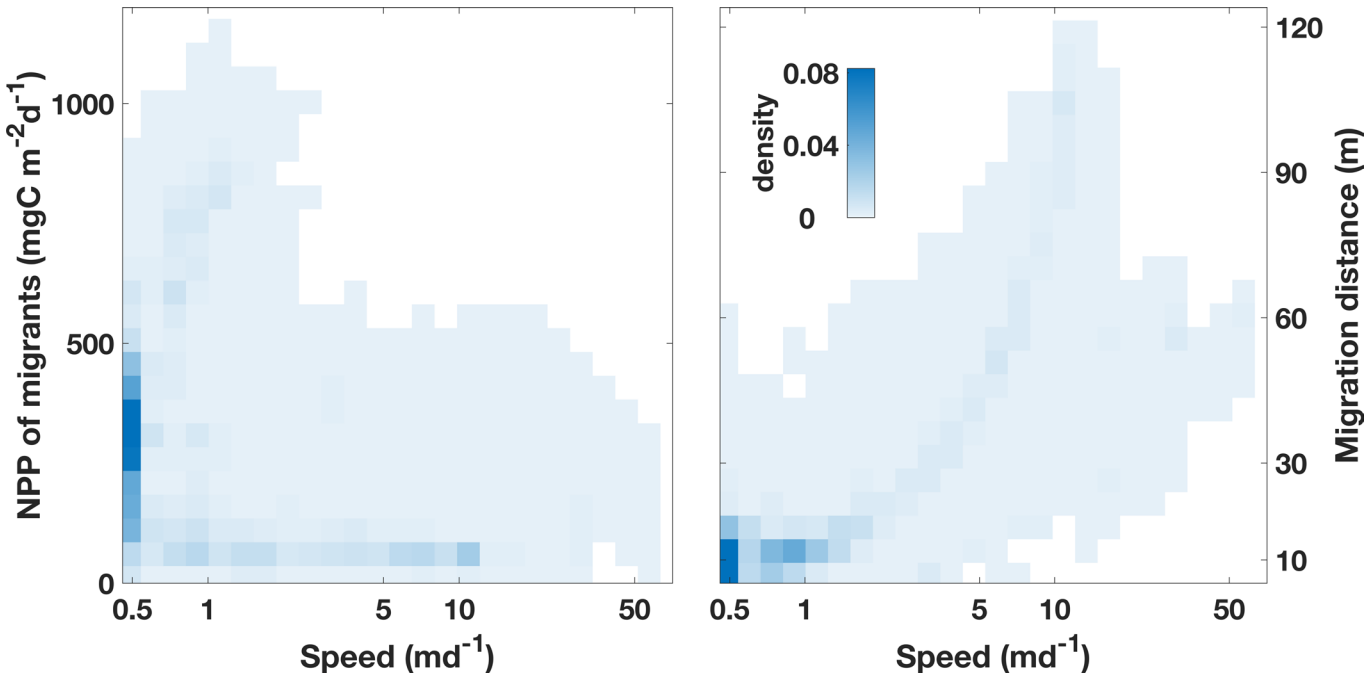

Extended Data Fig. 6 | Binned density distribution over the speeds of migrating phytoplankton *v*. Binned density distribution over the speeds of migrating phytoplankton *v*. As second variable, their NPP_{Σ} (left) and migration distance $2\delta z$ is chosen.

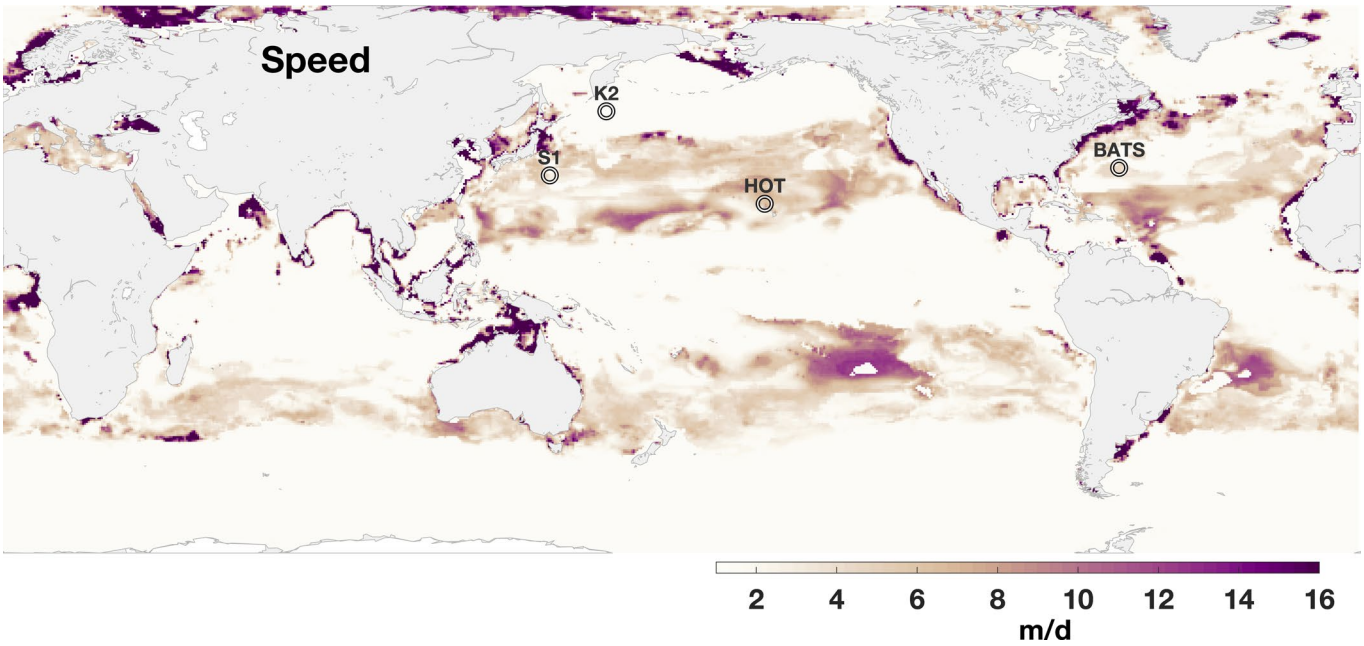

Extended Data Fig. 7 | Migration speed *v*. Migration speed *v* (annual mean of the average in the mobile community).

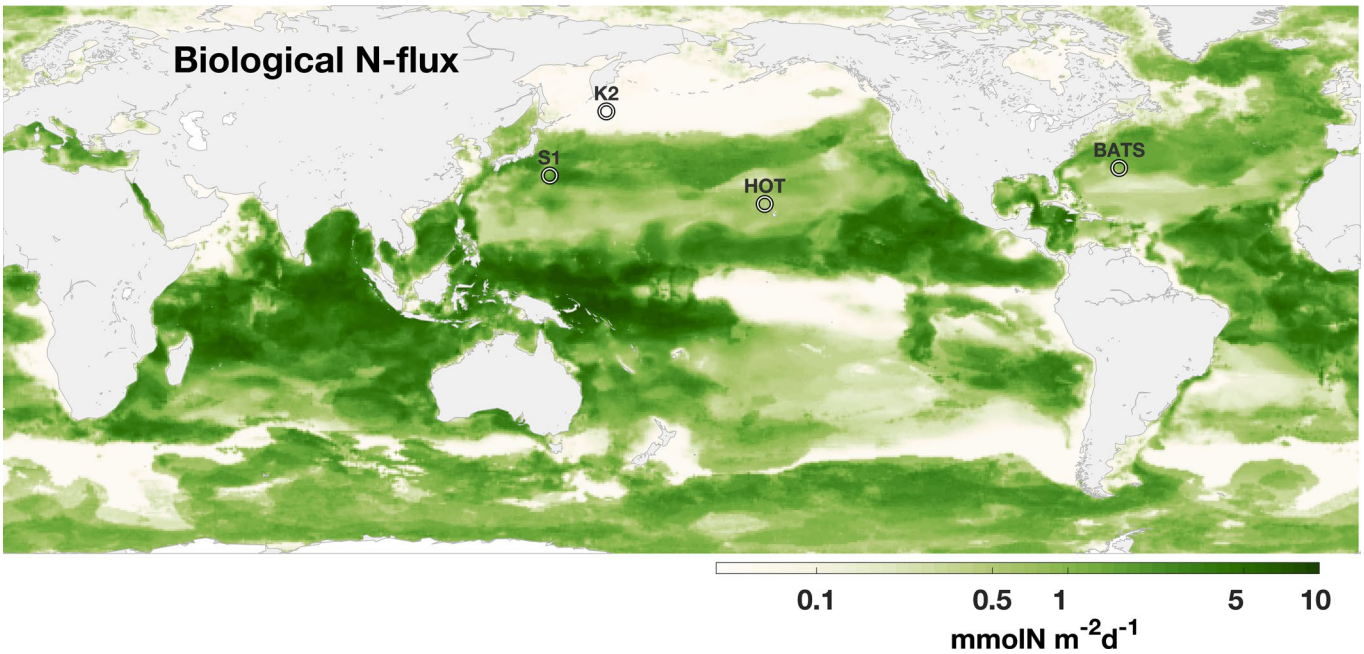

Extended Data Fig. 8 | Nitrogen upward transport flux induced by migrating phytoplankton. Nitrogen upward transport flux induced by migrating phytoplankton. The flux is estimated as depth integral above the chemocline over mortality rate of mobile phytoplankton times their nitrogen concentration.

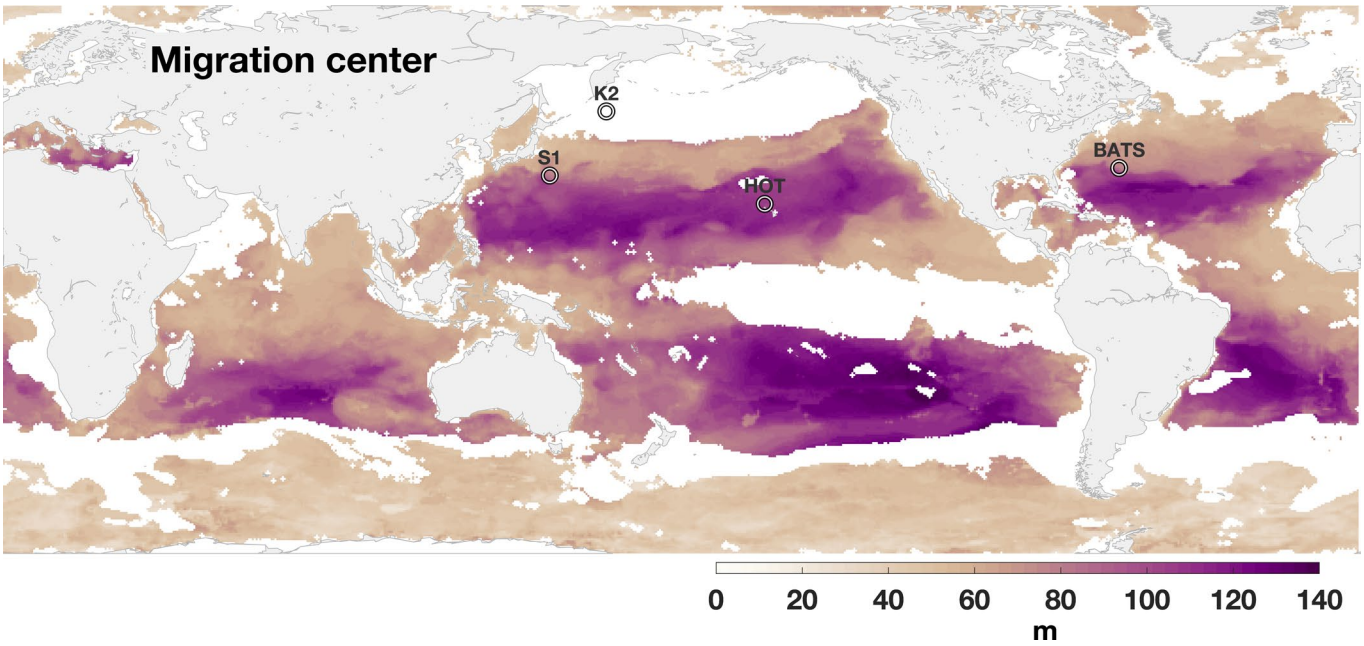

Extended Data Fig. 9 | Calculated center position of vertical cycles (z_{SCM}, annual mean). Calculated center position of vertical cycles (z_{SCM}, annual mean). z_{SCM} corresponds to the depth of the subsurface chlorophyll maximum (SCM). White areas indicate absence of vertical migration.

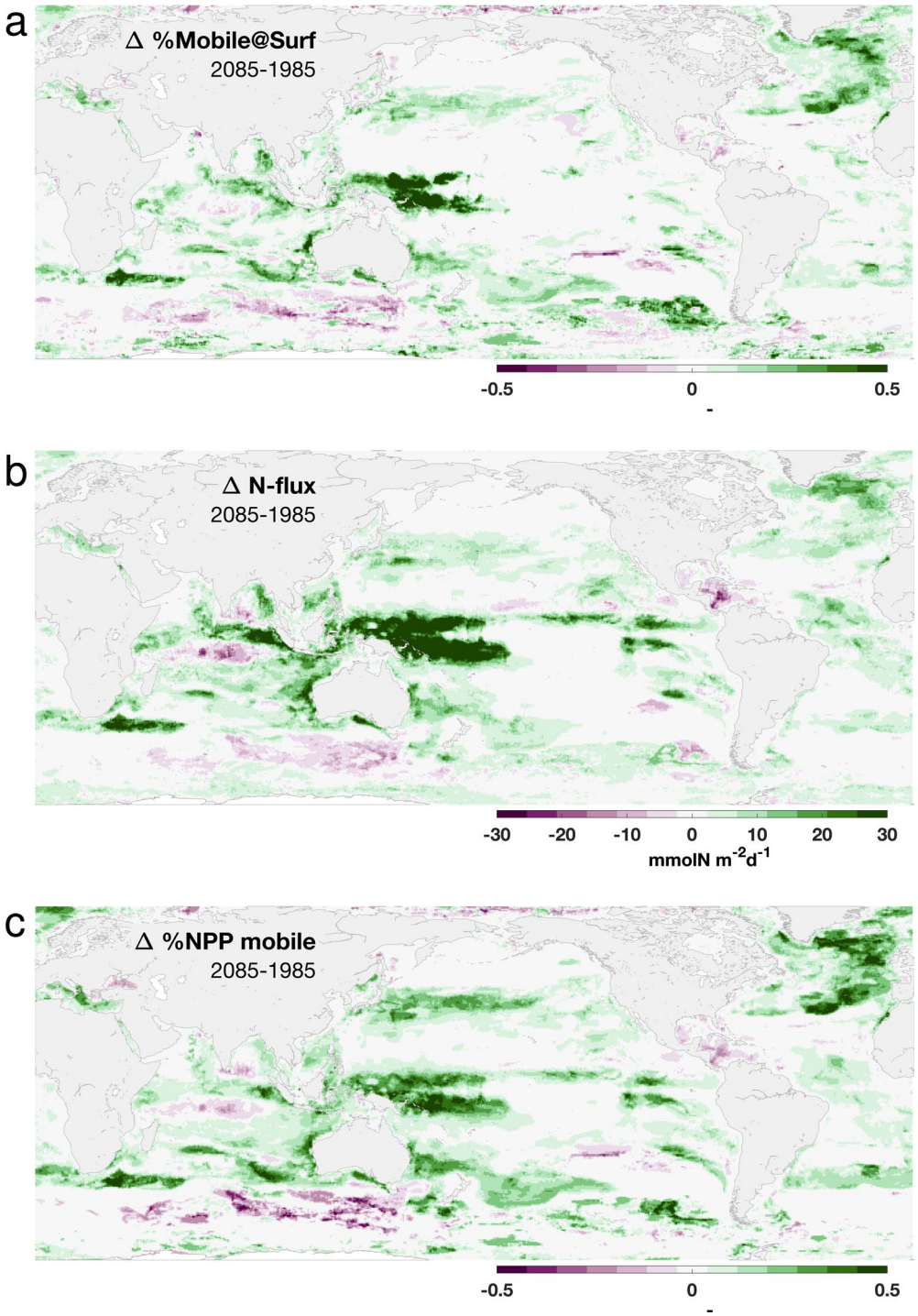

Extended Data Fig. 10 | Changes in model results in the climate change sensitivity experiment. Changes in model results in the climate change sensitivity experiment. a, Difference in the fraction of migrating phytoplankton in the surface layer (Δ %Mobile Surf, annual mean). The fraction for the reference chemocline distribution ('1985') is subtracted from the one after modification of z_N based on future changes in mixed layer depth as projected by a simulation of the Max-Planck-Institute Earth System Model ('2085'). b, Change in the nitrogen upward transport flux by migrating phytoplankton (Δ N-flux) from the reference simulation to the one with projected chemocline distribution. c, Concomitant change in the relative contribution of migrating phytoplankton to NPP_Σ (Δ %NPP mobile).